Structural and electronic properties of lithiated Si nanowires: An *ab initio* study

Teutë Bunjaku,[*] Dominik Bauer,[*] and Mathieu Luisier

Integrated Systems Laboratory, Department of Electrical Engineering and Information Technology,
ETH Zürich, Gloriastrasse 35, 8092 Zürich, Switzerland

Ab initio density-functional theory is used to study the structural changes of a crystalline silicon nanowire during lithiation and delithiation processes. Based on the obtained results quantum transport calculations are performed to shed light on the electrical current flowing at varying lithium concentrations. It is found that inserting lithium atoms into the crystalline silicon system leads to a steplike process, where each Si shell is successively lithiated from the outside. While increasing the Li concentration, the volume of the nanowire quadruples and the silicon network becomes fully amorphous. During delithiation the Li ions are initially homogeneously distributed throughout the nanowire cross section, eliminating the steplike behavior observed in the lithiation cycle. Hereby, the volume of the system decreases to 113% of its initial value, with a small amount of Li ions remaining in the Si network and a loss of storage capacity as a consequence. A simultaneous analysis of the current trajectories within the lithiated nanowires reveals that the main contribution shifts from the center to the surface of the nanostructure as the Li concentration increases.

I. INTRODUCTION

The Li-ion battery (LIB) technology has driven many industry sectors to huge success, particularly portable electronics [1–3]. Similarly, the race for renewable energy sources and long-range electrical vehicles has profited from the development of efficient energy storage units [4–7]. LIBs have already demonstrated promising results for these applications, but higher energy and power capacities as well as longer lifetimes are required to move to the next level of energy autonomy [4,7,8]. For all these reasons, the exploration of novel electrode materials with enhanced storage capabilities has become an intense research activity. Graphite, which is the most widely used anode material, is, for example, outperformed by silicon, the material of reference in the semiconductor industry, by a large margin; Si has a large theoretical specific capacity of about 4200 mAh/g, a value 10 times higher than graphite (372 mAh/g) [8,9]. However, large volume variations during the lithiation and delithiation processes lead to cracking of bulk Si, performance degradation, and a fatal reduction of the battery cycle life [6,10]. Alloying Si with other materials as well as patterning it into nanostructures have been shown to mitigate these issues [9,11,12]. In this context, the present work focuses on the characterization of the lithiation/delithiation of silicon nanowires (NWs) from first-principles. Although the advantage of Si nanowires over graphite has been experimentally demonstrated, theoretical investigations of the underlying physical mechanisms are still lacking. Further experimental developments might greatly benefit from a deeper understanding of the phenomena at play, not only those governing Li ion motions but also those affecting the resulting electrical transport properties.

Due to the crystalline nature of Si, the NW orientation can be crucial when it comes to the insertion of foreign atoms. Many groups [9,13–15] have examined several crystal orientations under lithiation. These studies have demonstrated that anisotropic swelling can occur in a NW with varying surface orientations. The $\langle 111 \rangle$-direction however, is characterized by six equal $\langle 110 \rangle$ surface planes, which are not only thermodynamically more favorable for fast initial ion diffusion [16], but also lead to quasi-isotropic volume expansions around the wire [9]. Thus, the focus of this work is set on this crystal configuration, its underlying processes and their outcomes, including the resultant electronic properties. Figure 1 depicts an exemplary structure of the investigated lithiated Si NWs. Instead of experimentally fabricating Si NW samples with different Li concentrations and characterizing them with complex experimental setups, an *ab initio* modeling approach based on density-functional theory (DFT) has been selected as inspection tool here. DFT is a well-established method to determine the suitability of a given material as battery electrode [17]. Recent progresses have been made possible by the availability of increased computational power and the development of advanced screening techniques [18–21]. Characterizing the potential of a possible electrode material comes down to the evaluation of several key features. This paper concentrates on the structural as well as on the electronic properties of Si NWs, as both critically affect the battery charge and discharge processes. The acquired knowledge will be useful to identify the optimal operating conditions of Si NWs as anode of LIBs.

The paper is organized as follows. Section II describes the simulation approach. In Sec. III the lithiation/delithiation of Si NWs is discussed, together with the resulting volume expansion/contraction and charge distribution. Finally, the electrical properties of lithiated Si NWs are analyzed before the paper is concluded.
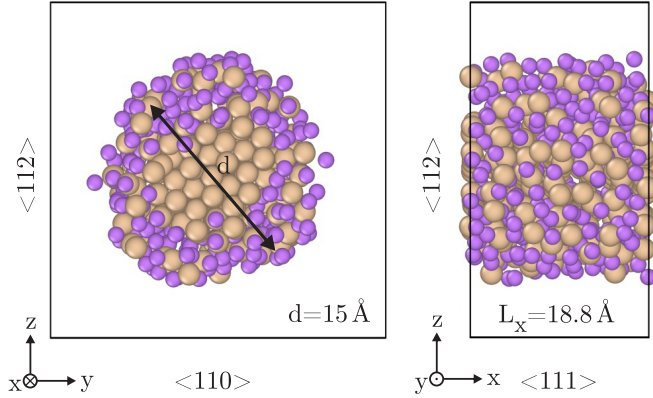
---

[*]These authors contributed equally to this work.

FIG. 1. Sample atomic configuration of $Li_{1.16}Si$. The purple and yellow spheres correspond to lithium and silicon atoms, respectively. The black box represents the simulated unit cell of the structure. The NW main axis is aligned with x.

II. SIMULATION APPROACH

The structural, ion diffusion, and charge distribution properties of Li_xSi ($0 \leqslant x \leqslant 4.4$) have been computed using DFT as implemented in the Vienna Ab Initio Software Package (VASP) [22,23]. Further transformations of the plane-wave results into maximally localized Wannier functions (MLWFs) have been realized with the Wannier90 tool [24]. The created atomic structures and the corresponding MLWFs allow us to compute the electronic current flowing through the considered systems with the help of a quantum transport solver.

A. Lithiaton/delithiation

As a starting point, a hexagonal crystalline Si NW has been constructed with a radius of 7.5 Å and a height of 18.8 Å along the $\langle 111 \rangle$ crystal orientation, resulting in six hexagonal sites facing the $\langle 110 \rangle$ direction. Due to the large distance between adjacent Si atoms, Lithium (Li) ions can easily move into the system and lithiate the Si NW quasi-isotropically [9]. Other NW growth directions have not been included in this study, because of the computational cost of the considered method. The crystalline NW has been created using Virtual NanoLab (VNL) [25] and the Li atoms have been introduced into the structure by passivating the surface of the system. This has been performed using the sp3 hybridization of Si, and replacing the hydrogen with Li atoms.

The atomistic calculations have been done using the projector-augmented wave method [26] and the local density approximation (LDA) exchange correlation functional. The cutoff energy for the plane-wave basis set has been set to 550 eV and for all simulations, the k-point sampling has been restricted to the Γ-point. For the structural calculations, convergence has been considered to be achieved when the energy difference between two consecutive steps reaches a value of 10^{-5} eV and the force acting on each ion becomes smaller than 10^{-3} eV/Å. The initial Si NW unit cell consists of 220 Si atoms. From 1 to 968 Li atoms have been continuously added to the system. The NW has been embedded within a cubic cell large enough to avoid any possible interactions with its neighboring periodic replicas. Starting with an initial cubic

cell size of (18.8 Å, 30 Å, 30 Å) and continuously increasing its y and z length until reaching (18.8 Å, 55 Å, 55 Å) at $Li_{4.4}Si$.

After passivating the Si NW with Li, the constructed crystal structure has been optimized by relaxing the initial energy with the conjugate gradient algorithm [27]. The kinetics of the system have been monitored, performing thorough molecular dynamics (MD) simulations using a Nose-Hoover thermostat with a step size of 1 fs. For the MD calculations a temperature profile of $T = (750 \text{ K}, \ 500 \text{ K})$ has been employed and the structure has been considered stable if it stays in the same potential energy surface minimum after undergoing 3 ps of high temperature MD. After reaching this lowest energy configuration, the surface of the NW has been again passivated with Li atoms, and a structure with an increased Li concentration has been created. The resulting configuration has been once more subject to a high temperature MD run, and the surface of its lowest energy structure has been passivated with Li atoms. This process consisting of (i) Li surface passivation and (ii) MD runs with their corresponding minimization steps has been repeated until the Li storage capacity of the Si-NW is reached, in the present case, when 968 Li atoms have been added.

During the annealing process of each considered Li concentration, the atomic positions have been extracted and minimized after every picosecond to obtain intermediate configurations before reaching the final and most stable arrangement of each concentration.

The structural and volumetric changes of the material have been evaluated by constructing a polyhedral mesh of the whole NW at various Li concentrations and comparing it to the initial configuration using ovito [28].

While increasing the number of Li atoms in the system, it is crucial to monitor the binding energy $E_b(Li_xSi)$, as shown in Refs. [29,30],

$$E_b(m) = \frac{E_n - (E_{n-m} + mE_{Li})}{m}, \qquad (1)$$

where E_b is the average relative binding energy for each of the m newly introduced Li atoms, E_n is the total energy of the structure when n Li atoms are present, and E_{Li} is the cohesive energy of a Li atom in a body-centered cubic (bcc) bulk structure. To ensure that no overcharging occurs, the condition $E_b(Li_xSi) < 0$ has to be fulfilled at all times.

Apart from the binding energy, the electrode open circuit voltage (V_{oc}) has been calculated [31] using the following equation:

$$V_{oc} = -\frac{E_{Li_{x_1}Si} - E_{Li_{x_2}Si} - (x_1 - x_2)E_{Li}}{(x_1 - x_2)e}, \qquad (2)$$

where $E_{Li_{x_1}Si}$ and $E_{Li_{x_2}Si}$ are the total energies of the lithiated systems at concentrations x_1 and x_2, respectively, and E_{Li} is the cohesive energy of a Li atom in a bcc bulk structure, as V_{oc} is calculated with respect to metallic Li. During the lithiation process, the value of x_2 has been set to zero, and x_1 has been continuously increased until reaching $Li_{4.4}Si$.

In addition to the open circuit voltage, the theoretical specific capacity C has been determined at various Li

concentration levels according to

$$C = \frac{n \times F}{m}. \quad (3)$$

In Eq. (3) n is the number of electrons transferred at each concentration ($0 \leqslant n \leqslant 4.4$), F the Faraday constant, and m the molecular weight of the active material. Using this expression, the theoretical capacity reaches a value of 4200 mAh/g, comparing very well to previous experimental works [32,33]. By combining the two equations above, the open circuit voltage can be evaluated at different capacity levels instead of Li concentration.

To further understand the lithiation process of the Si-NW, single Li movements inside the Si network have been investigated. Using the lowest energy configuration at each Li concentration, the next diffusion steps and their corresponding energy barriers have been determined by means of nudged elastic band (NEB) calculations [34]. A NEB consisting of seven images has been created based on the image-dependent pair potential method [35]. Therefore, the final NEB calculation setup involves an initial and final state, as well as seven images representing intermediate structures between these two configurations. The *climbing image NEB* has been assumed converged when the energy difference between two consecutive iterations has become smaller than 10^{-3} eV.

Finally, the changes in the charge distribution has been studied through a Bader analysis [36]. This allows one to characterize the transfer of charges at different stages of the lithiation process and observe the interaction between the Si and Li atoms.

After reaching a concentration of $Li_{4.4}Si$, where the Si NW is lithiated to its core, the delithiation process has been initiated by randomly removing the Li atoms sitting on the surface of the NW. At each delithiation step, ten structures have been constructed. In each of them 90% of the Li atoms lying in a 3 Å shell from the surface have been randomly removed. Each of these ten structures has gone through an initial minimization step, and the lowest energy configuration has been subject to further MD calculations, which can be adopted from the lithiation process as they stand. A structure has been considered stable if it has not left its current minimum on the potential energy surface after 3 ps of high temperature MD. This delithiation scheme has been repeated until the Li ions do not move to the surface of the NW anymore, but rather stay inside the host material. At this point the delithiation process has been terminated and no further step has been performed. The influence of surface stress has not been studied in this work, but interested readers are referred to Refs. [14,15].

B. Electronic part

To analyze the electron current flow through the previously generated structures, a finite system is needed where electrons can be injected on one side and transmitted to the other. Therefore, the Bloch-like Hamiltonian, which is produced by VASP for a periodic cell, has been transformed into a set of maximally localized Wannier functions (MLWFs) with the Wannier90 tool [24] using one WF for Li (s-like) and four WFs for Si (s- and p-like). The MLWF-Hamiltonian includes all interactions between neighboring orbitals (Wannier

functions) within a cutoff radius of 18.8 Å. To do that, the NW structures have been extended along the transport direction x in Fig. 1, which leads to the formation of a block tridiagonal Hamiltonian matrix. The latter has then been utilized within a ballistic quantum transport solver based on the wave function (WF) or nonequilibrium Green's function (NEGF) formalism [37] to obtain the current I_d between two atoms i and j [38],

$$I_{d,ij} = \frac{2e}{\hbar} \sum_{k,\sigma_1,\sigma_2} \int \frac{dE}{2\pi} \left[H^{\sigma_1 \sigma_2}_{\mathrm{MLWF}_{ij}}(k) G^{<\sigma_2 \sigma_1}_{ji}(E, k) \right. $$
$$\left. - G^{<\sigma_1 \sigma_2}_{ij} H^{\sigma_2 \sigma_1}_{\mathrm{MLWF}_{ji}}(k) \right], \quad (4)$$

where $H^{\sigma_1 \sigma_2}_{\mathrm{MLWF}_{ij}}(k)$ is the momentum-dependent Hamiltonian matrix element between atoms i and j and Wannier functions σ_1 and σ_2, $G^{<\sigma_1 \sigma_2}_{ij}(E, k)$ the lesser Green's function coupling atoms i and j as well as Wannier functions σ_1 and σ_2 at energy E and momentum k, e the elementary charge, and $\hbar$ Planck's reduced constant. Due to quantum confinement along the y and z axes of the NW, only the Γ-point needs to be accounted for, i.e., $k = 0$, and the sum over k disappears. To drive the considered structures out-of-equilibrium, a small voltage difference $\triangle V \leqslant 1 \times 10^{-3}$ V has been applied between the two ends of the nanowires. This value ensures that we remain in the linear regime where $I_d \sim G_{\mathrm{el}} \triangle V$ and the electrical conductance G_{el} does not depend on $\triangle V$. These calculations do not only allow to extract the total current flowing through the simulated NWs, but also to establish the contributions coming from each individual atom. More details about this approach can be found in Ref. [39]. The consideration of inelastic phonon interactions is computationally too expensive given the size of the studied structures, which is why this work is restricted to the ballistic case.

III. RESULTS

A. Structural and volume changes

The insertion of Li atoms inside a crystalline Si NW induces large changes in its atomic structures and results in high volume expansions. The structural variations can be best visualized by calculating the radial distribution function (RDF) of Si-Si, Li-Li, and Si-Li pairs. The RDF $g(r)$ measures the probability of finding a particle at distance r, given that there is a particle at position 0 [28]. Thus, by precisely identifying the peaks of these distributions, nearest neighbor distances between different atomic pairs can be determined.

Figure 2(a) shows the RDF of Si-Si at four different Li concentrations, namely Si, $Li_{2.2}Si$, $Li_{4.4}Si$, and $Li_{0.13}Si$. The shortest distance between pairs of Si atoms does not significantly change upon lithiation, but rather stays between 2.375 Å and 2.475 Å. The distance to the second nearest-neighbors, however, strongly varies during the lithiation/delithiation process. For the crystalline Si NW the peak is prominently placed at 3.825 Å and shifts toward 4.325 Å when reaching the end of the lithiation process. This increase in second nearest-neighbor distance can be explained by the large number of Li atoms introduced into the system and thus causing the Si atoms to move further apart from each other. The distances to the first and second nearest-neighbors fall back to their original values (1st peak, 2.375 Å; 2nd peak,
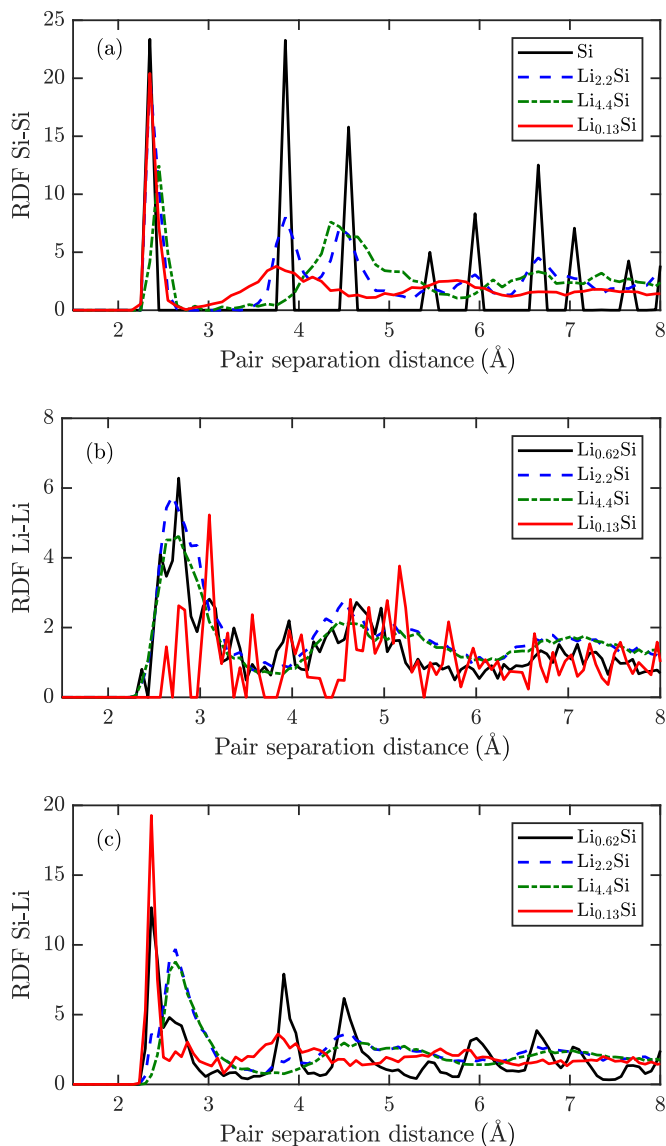
FIG. 2. Radial distribution function of (a) Si-Si, (b) Li-Li, and (c) Si-Li pairs. The vertical axis represents the probability of finding a particle at a distance r, given that there is a particle at position 0. The RDF is thus a probability function without a unit. In each case, four Li concentration levels are examined, three of which during the lithiation of the NW ($Li_{0.62}Si$, $Li_{2.2}Si$, $Li_{4.4}Si$) and one at the end of the delithiation ($Li_{0.13}Si$).

3.775 Å) after the Li atoms have been removed from the Si network and the system is fully delithiated. At this stage the Si network is fully amorphous and no crystalline structure can be identified in the RDF. The sharp peaks corresponding to second, third, fourth, etc. nearest-neighbors have either widened or vanished.

The RDF for Li-Li pairs is shown in Fig. 2(b). Distribution changes upon lithiation/delithiation are only minor. The nearest-neighbor distance decreases slightly from 2.71 Å to 2.66 Å upon lithiation and increases to 3.033 Å when the system is fully delithiated. Still, this increase can be attributed to the small number of Li atoms remaining inside the NW
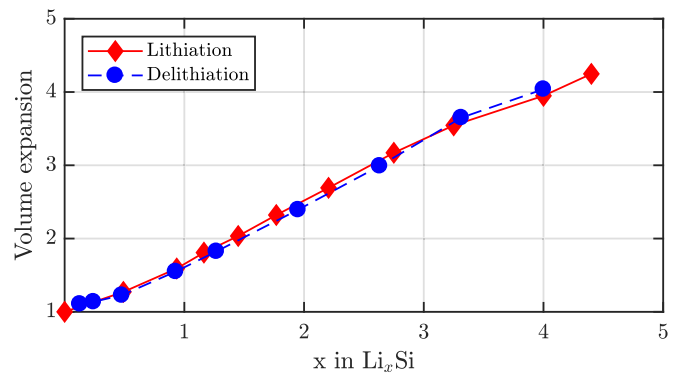

FIG. 3. Volume expansion/contraction of the Si NW upon lithiation/delithiation. The solid red line with diamonds represents the values during lithiation, while the blue dashed line with circles refers to the delithiation case.

after full delithiation, which enables them to spread out inside the amorphous Si system.

The nearest-neighbor distances between Si-Li pairs can be seen in Fig. 2(c). The first peak (nearest-neighbor distance) shifts from 2.367 Å to 2.633 Å upon lithiation, but falls back to the value found for $Li_{0.49}Si$ after the Si NW has been fully delithiated ($Li_{0.13}Si$).

The radial distribution functions determined here for the lithiated Si NW compare fairly well to the Si-Li and Li-Li nearest-neighbor distances of bulk $Li_{15}Si_4$ [40], where the values were determined to be 2.62 Å for Li-Si and 2.65 Å for Li-Li pairs (here, 2.633 Å and 2.66 Å, respectively).

Apart from the RDF, the volume changes upon lithiation and delithiation have been computed. They can be visualized in Fig. 3. The volume expansion and contraction exhibits a linear behavior with respect to the Li concentration. These quantities have been determined as a ratio between the current (V_x for Li_xSi) and initial (V_0 for Si) NW volumes ($\frac{V_x}{V_0}$). Both curves lie almost on top of each other. The Si NW increases by up to 420% during the lithiation process and then decreases again until reaching 113% of its initial volume at $Li_{0.13}Si$. The volume expansion compares fairly well to previous experimental measurements, where a volume increase of 400% has been observed [6]. At the end of the delithiation process the Si NW still hosts Li ions, implying a loss of energy storage capacity after the first cycle.

After this initial lithiation and delithiation, the crystalline structure of the Si NW disappears. It is replaced by an amorphous phase that is clearly visible in the RDF presented in Fig. 2(a).

B. Binding energy and open-circuit voltage

As the next step, the lithiation process and the movement of the Li ions inside the Si NW have been studied at different Li concentration levels. Starting with the pure crystalline Si NW, a first sp3 passivation of the surface has been performed leading to $Li_{0.49}Si$. The introduced Li atoms adhere to the two outmost hexagon shells of the Si NW, leaving the core of the Si network unperturbed and still in its crystalline form. Forcing the Li atoms further into the system is not possible as this results in an energy increase, and thus in an energetically
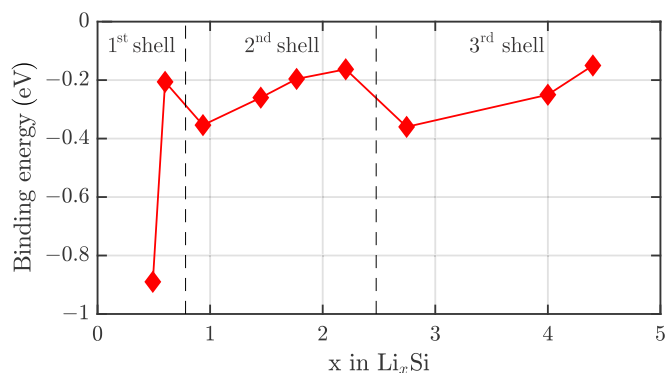
FIG. 4. Binding energy of the Li ions to the Si NW. The values have been determined for Li concentrations from $Li_{0.49}Si$ to $Li_{4.4}Si$. The two dashed vertical lines represent the penetration of the first Li ions into the next Si hexagon shell of the NW.

less favorable configuration. This initial calculation suggests that the NW will not be homogeneously lithiated, but rather shell by shell. Further calculations at higher Li concentrations have confirmed this hypothesis.

While increasing the Li concentration and determining stable atomic configurations for all the desired concentration levels, the binding energy of the Li ions has been constantly monitored. Figure 4 shows this energy for Li_xSi, where x lies in the range (0,4.4). The two vertical dashed lines indicate the concentrations at which Li ions start penetrating into the next Si hexagonal shell. As initially observed for $Li_{0.49}Si$, the Li ions move inside the host material shell by shell and act as a front propagating toward the center of the Si NW. This behavior can be clearly seen in Fig. 5, where the Si and Li densities are shown for various Li concentrations as a function of the distance from the NW core. At the lowest lithiation level ($Li_{0.49}Si$) the largely intact crystalline structure of the NW is recognizable by the four peaks present in subplot Fig. 5(a), each of them corresponding to a different hexagonal Si shell. When the amount of Li in the system increases, these peaks broaden and a dissolution of the hexagonal shells is observed, one after the other, starting from the outside. At $Li_{4.4}$, no distinct maximum can be identified in the density anymore, implying a more homogeneous Si distribution.

The distribution of the Li ions can be analyzed in Fig. 5(b), all along the lithiation process. Each time a Si hexagonal shell breaks up, the Li density increases at this location and a distinct maximum is observed in the density plot. Similar to the Si case, these peaks broaden and a more homogeneous Li distribution is obtained at the end of the lithiation process.

The observed stepwise lithiation mechanism is most likely caused by the stress present at the Li to crystalline Si interface. Before a Si hexagonal shell can be broken, the Si-Si bonds at the surface must be weakened, which usually occurs via charge transfer from the Li ions to the Si atoms [41]. When Li atoms are introduced into the Si NW, they transfer roughly 80% of their charge to the surrounding Si atoms, going from Li to Li^+. Due to this charge intake, the Si-Si bonds weaken and the diffusion of Li ions between two Si atoms becomes feasible. A locally increased number of Li atoms leads to more charges transferred to the Si particles, causing a more
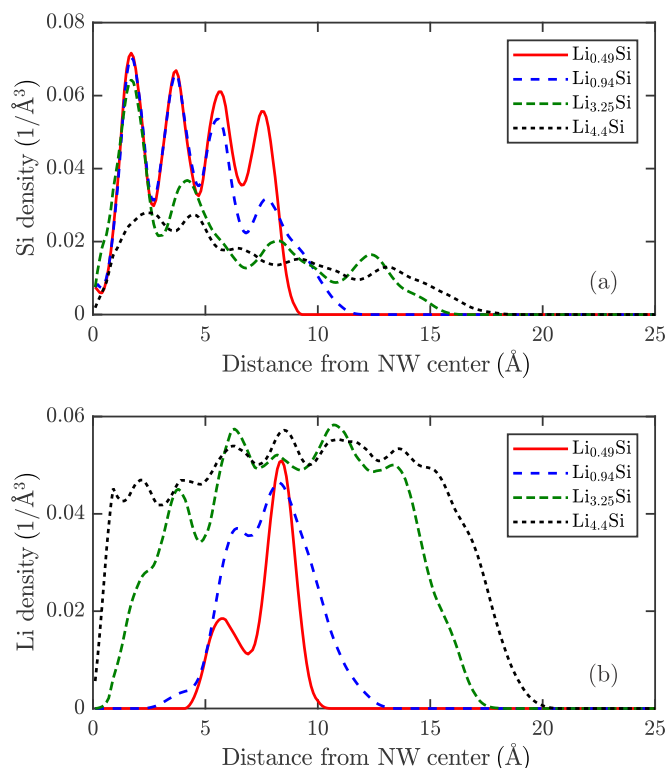

FIG. 5. Volumetric density of the (a) Si and (b) Li atoms at different lithiation levels ($x = 0.49, 0.94, 3.25, 4.4$) as a function of the distance from the NW center.

significant weakening of their nearest-neighbor bonds. This enables the Li ions to penetrate into the highly crystalline Si network. In other words, the Li concentration must reach a threshold before the next Si hexagon shell can be attacked.

The penetration of Li ions into the next hexagonal shell can be additionally observed in Fig. 4, where the binding energy for the penetration of each shell starts at a very low value and continuously increases upon lithiation. Right before the Li ions move further into the next hexagonal shell, the binding energy strongly increases until reaching a value close to 0 eV. Immediately after, the next shell becomes lithiated and the binding energy decreases and reaches a minimum. At $Li_{4.4}Si$ the storage capacity of the host material is full and no additional Li atom can be inserted.

After the Si NW has been fully lithiated, the delithiation process has been initiated. The initial distribution of the Li ions is more homogeneous due to the amorphous nature of the Li_xSi compound. It has been found that shortly after the surface Li atoms are removed, the remaining Li particles rearrange themselves, giving rise to the above-mentioned homogeneous Li distribution throughout the NW cross section.

Apart from the binding energy, the open-circuit voltage (V_{oc}) and the theoretical specific capacity of the lithiated Si-NW have been calculated during the lithiation and delithiation process using Eqs. (2) and (3). The results are given in Fig. 6. While lithiating the Si NW the voltage drops from 0.85 to 0.3 V. During the delithiation process the open-circuit voltage increases from 0.3 to 1.1 V. The previously discussed slight loss in storage capacity can be clearly observed in Fig. 6,
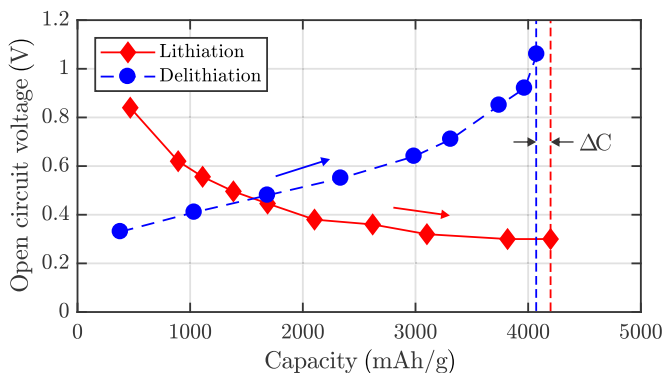
FIG. 6. Open circuit voltage (V_{oc}) during the lithiation (red diamonds on solid line) and delithiation (blue circles on dotted line) process, as a function of the storage capacity. The red dashed line represents the maximum storage capacity reached after the first lithiation cycle, whereas the blue line shows the Li storage capacity after the delithiation process.

where the capacity after the full delithiation process does not reach its initial value anymore. This difference is indicated by the two vertical dashed lines in Fig. 6, which show the maximum capacity after the first lithiation (red line) and delithiation (blue line) process. The gap in between them represents the capacity loss $\Delta C = 122$ mAh/g, roughly 3% of the overall capacity.

C. Charge transfer and NEB

During the lithiation process, the Si and Li atoms transfer part of their charge to their surrounding neighbors. Figure 7 shows the charge distribution of the Si atoms at different Li concentration levels. At $Li_{0.49}Si$, the charge sitting on each Si atom ranges between 0e and 1e, whereas the Li atoms have donated $0.76e$ to $0.82e$ to their neighboring atoms, becoming Li^+. While the surface Si atoms receive charges from the surrounding Li ions, the core of the NW remains unaffected and quasi neutral. This behavior corresponds to a local charge transfer as opposed to a delocalized distribution of the charges over the whole Si network, as observed in the lithiation of Si nanoclusters [42]. Examining the charge distribution for $Li_{2.2}Si$ reveals that the crystalline, unlithiated core has become smaller, surrounded by a highly amorphous and lithiated outer shell. These results are depicted in Fig. 7(b). A large spread of charge on the Si atoms $[0.2e, 3.8e]$ can be observed, whereas the charge on the Li ions is very narrow $[-0.78e, -0.80e]$, as previously observed in Ref. [42]. The core of the Si network preserves its initial charge and is not strongly affected by the introduced Li atoms. Finally, the fully lithiated Si NW ($Li_{4.4}Si$) is shown in Fig. 7(c). The charge distribution on the Si atoms ranges between 0.6e and 4.8e as the crystalline core of the NW has been lithiated too and the Si network has become fully amorphous. Despite the large spread of the charge distribution on the Si atoms, regardless of the lithiation level, the range of the charges donated by the Li atoms remains narrow $[0.75e, 0.79e]$. The variance of the Si charge distribution continuously increases upon lithiation until the last hexagon layer is lithiated at $Li_{2.75}Si$ (see Fig. 4). Following this threshold, further lithiation does not increase
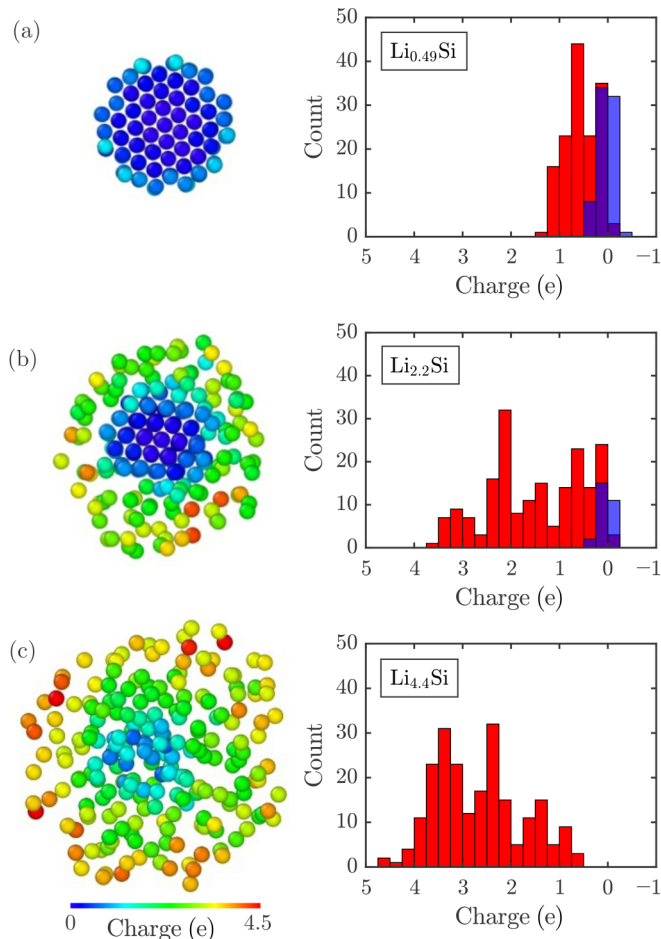

FIG. 7. Charge distribution for the Si atoms in $Li_{0.49}Si$, $Li_{2.2}Si$, and $Li_{4.4}Si$. On the left, the charge on each atoms is shown for the three structures. On the right, it is visualized in histogram form, where the red bars represent the charge outside the crystalline core and the blue bars show the charge distribution for the atoms inside the crystalline core.

the variance of the charge located on each Si atom anymore, but rather leads to a more homogeneous distribution.

After the Si NW has been fully lithiated, the delithiation process can start by removing Li ions at the NW surface. As previously mentioned, the delithiation is a more gradual process because the Li ions are homogeneously distributed over the Si network. Due to this feature, the range over which the charges on the Si atoms vary decreases. The mean charge per Si and Li particle as well as the variance of both quantities are reported in Table I for the delithiation process, confirming this observation.

In addition to the charge distribution, the energy barriers for the diffusion steps at five Li concentration levels (Li_xSi, $x = 0.49, 0.71, 0.94, 1.77, 2.2$) have been examined. The barriers are shown in Fig. 8(a) and the corresponding hexagonal shells being lithiated are depicted in Fig. 8(b). The two dashed lines shown in Fig. 8(a) represent the penetration of the first Li ions into the next Si hexagonal shell of the NW. As mentioned in Sec. III B, the Li ions weaken the Si-Si bonds, which enables them to diffuse further into the NW. This behavior is highlighted in Fig. 8, where a continuous decrease of the

TABLE I. Average charge on each Si atoms and Li ion [e] together with the corresponding variance.

x in Li$_x$Si	Q_{Si}		Q_{Li}	
	Avg.	Var.	Avg.	Var.
3.3	2.41	0.57	0.73	0.02
2.6	1.99	0.32	0.76	10^{-5}
1.95	1.49	0.22	0.77	10^{-5}
1.27	0.99	0.13	0.78	10^{-5}
0.48	0.38	0.05	0.81	10^{-5}
0.13	0.10	0.02	0.81	10^{-5}

FIG. 9. (a) Hydrogen-passivated Si NW and (b) Li$_4$Si structure. On the left-hand side the atomic configurations are depicted. White, purple, and yellow spheres correspond to hydrogen, lithium, and silicon atoms, respectively. On the right hand side the same structure is overlaid with the absolute current flowing through each atom along the NW axis (out-of-plane axis), ranging from the highest current in red to the lowest one in blue.

diffusion barrier height can be identified for the two examined shells. The energy needed to fill the two shells decreases with increased Li concentration until finally penetrating the next Si hexagon. At this point, the barrier height for Li diffusion abruptly increases until the Li concentration becomes large enough to attack the next shell. The lower energy barriers at increased Li concentrations are a direct consequence of the charge transfer from the Li to the Si atoms and its induced weakening of the Si-Si bonds. This bond weakening leads to a more favorable Li diffusion and thus decreased energy barrier. Hence, the computed Li binding energy, Li-Si charge transfer, and Li diffusion barrier height, point all toward a steplike movement of Li into crystalline Si NWs. Although molecular dynamics simulations at various temperatures and over longer times could be really useful to confirm the obtained diffusion barrier heights, the available computational resources did not allow us to do so.

It should be noted that in case of amorphous structures, concerted Li ion motions could take place that are not captured by NEB [43]. Here, we apply NEB at the boundary between a crystalline core and amorphous shell so that concerted atomic motions are expected to play a minor role.
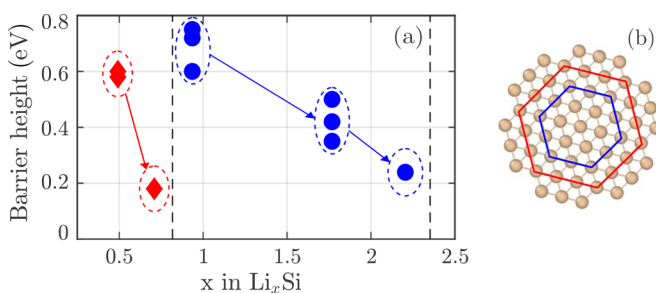

FIG. 8. NEB calculations and the resulting (a) energy barrier heights for five different Li concentrations are shown. In (b) the crystalline Si-NW and the two examined Si shells are visualized. At each concentration one to three diffusion steps and their corresponding energy barriers have been calculated. The two vertical lines in (a) represent the first Li ions penetrating into the next Si hexagonal shell. The red diamonds show the barrier heights for the diffusion steps at the second shell, wheres the blue circles show the values for the third Si hexagon shell.
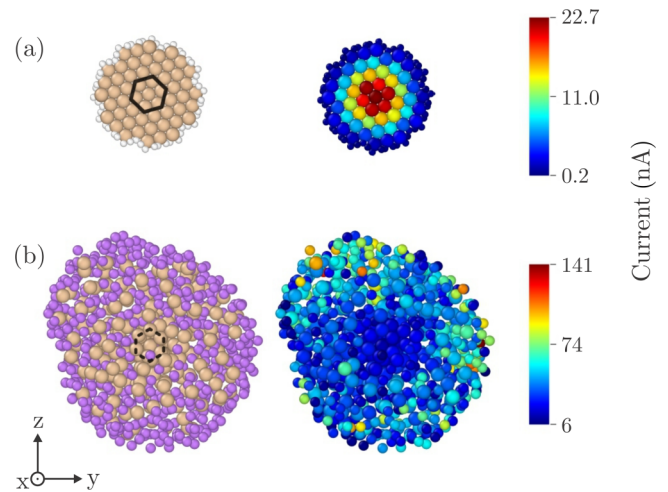
D. Electrical current analysis

As electrons must be captured/released during the lithiation/delithiation processes, it is also important to study the electrical properties of Li$_x$Si NWs and shed light on the mechanisms that affect the current flows. Quantum transport simulations, as described in Sec. II, have therefore been performed along the NW axis (x) at each Li concentration. In addition, a pure crystalline Si NW has been analyzed as a reference. In this case, the NW surface has been passivated with hydrogen atoms, as depicted in Fig. 9(a). The ordered atomic arrangements as well as the repetitive hexagonal shells around the center are clearly visible. The right side of Fig. 9(a) shows the current distribution flowing through this NW structure. With the help of Eq. (4), the current between two orbitals (Wannier functions) belonging to two neighbor atoms can be evaluated, summed up, and attributed to the atom it originates from. The color indicates the current magnitude, red when it is high, blue when it is low. For crystalline Si NWs of low diameter, the maximum of the current is located in the center, as can be seen in Fig. 9(a). Note that the Fermi energy has been set to the conduction band edge to emulate the presence of doping atoms within the NW. In the undoped case, no current would flow. For the remaining lithiated Si NWs, the Fermi level extracted from the DFT calculation is used, i.e. assuming charge neutrality. Figure 9(b) displays the current distribution for the Li$_4$Si structure, where the entire Si network is lithiated. Besides the transition from a crystalline NW to an amorphous one, which is accompanied by a disappearance of the hexagonal shells, a radical change in the current distribution can be observed as well. Compared to Fig. 9(a), the atoms in the center of the NW contribute the least to the overall current. Atoms scattered around the center and positioned close to the surface carry most of the current. Also, due to the metallic nature of Li$_4$Si and the larger
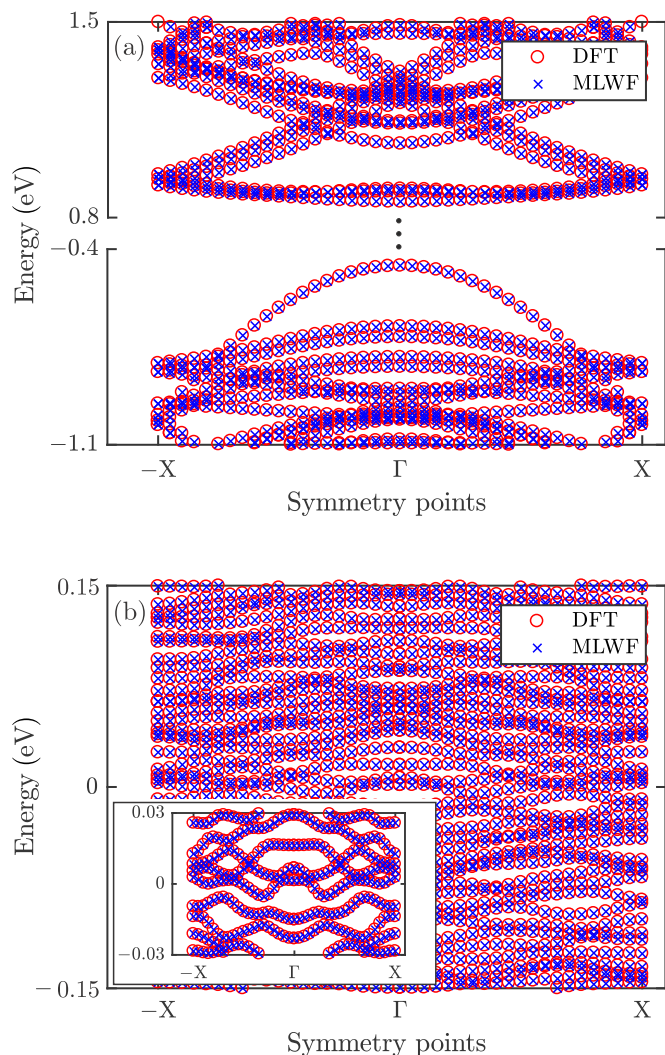
FIG. 10. Bandstructures of (a) hydrogen passivated silicon and (b) Li$_4$Si along the transport direction (x). The red circles refer to DFT results, the blue crosses to the MLWF representation. Note that the bands are shifted, so that the respective Fermi level coincides with zero.

FIG. 11. Radial current analysis for (a) Li$_{1.45}$Si, (b) Li$_{2.75}$Si, and (c) Li$_4$Si. The purple and yellow spheres on the left correspond to lithium and Si atoms, respectively. The color bars on the right refer to the computed average current along the NW axis in each delimited ring. The inner hexagon/ring has a diameter of 6 Å. All the other rings have a thickness of 3 Å.

cross section, the current is about one order of magnitude larger than in a highly doped Si NW. To illustrate this, Fig. 10 compares the band structure of these two cases. It can be seen that the insertion of metallic Li closes the band gap, which is present in a hydrogen passivated Si NW. The noticeable decrease of the bandgap leaves no doubt about the transition, even when taking the known bandgap underestimation of the LDA approximation into account [44,45]. In addition, it shows that the MLWF representation agrees very well with the DFT results.

From the previous sections, it is known that Li ions penetrate into the Si NW shell after shell, breaking up Si bonds in the process. This is why a radial analysis of the current appears more suitable to extract relevant information. This has been done by dividing the cross section of the NW into several rings of 3 Å thickness around the central hexagon. The current flowing through each atom present in a given ring has then been summed up and averaged over the number of atoms,
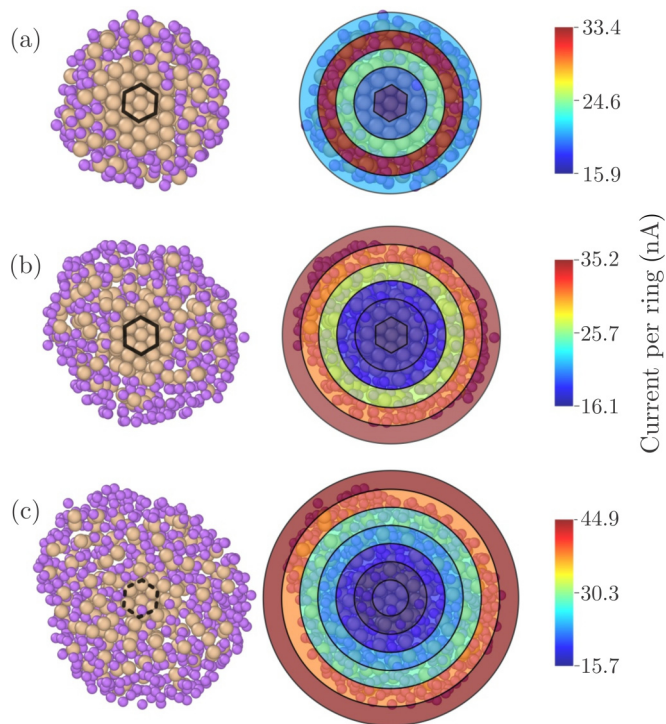
which determines the ring color. Figure 11 illustrates this analysis for three exemplary configurations, Li$_{1.45}$Si, Li$_{2.75}$Si, and Li$_4$Si. On the left-hand side, the atomic structures are shown, whereas on the right-hand side, the current per ring is depicted. For the lower lithiation levels, ($x = 1.45$ and 2.75), the crystalline core remains intact, as highlighted by the presence of a well-ordered hexagon in the center of the NW. When comparing the current rings in Fig. 11, it can be observed that the current avoids the NW center, even in the case of a crystalline core. Regions with high current contributions are situated close to the surface, where lithium has been inserted between Si atoms. It is apparent that the maximum of the current tends to move away from the NW center as the Li concentration increases, and preferably flows through Li-rich, quasi-metallic regions. Hence, it can be concluded that the insertion of reactive Li ions causes the favorable electron conductance region to shift from the core toward the surface, making it more sensitive to surface defects and roughness that have not been considered here.

Figure 12 presents a different view on the radial distribution of the current for an increasing lithium concentration. From there, a direct correlation between the number of atoms per ring and the average electrical current flowing through it can be established. First, it should be noted that the lowest lithiated Si NW Li$_{0.49}$Si features a quasi-insulating behavior. Here, the presence of a band gap due to the semiconductor nature of Si prevents a larger current. The comparatively low concentration of lithium is not able to lift the Fermi energy
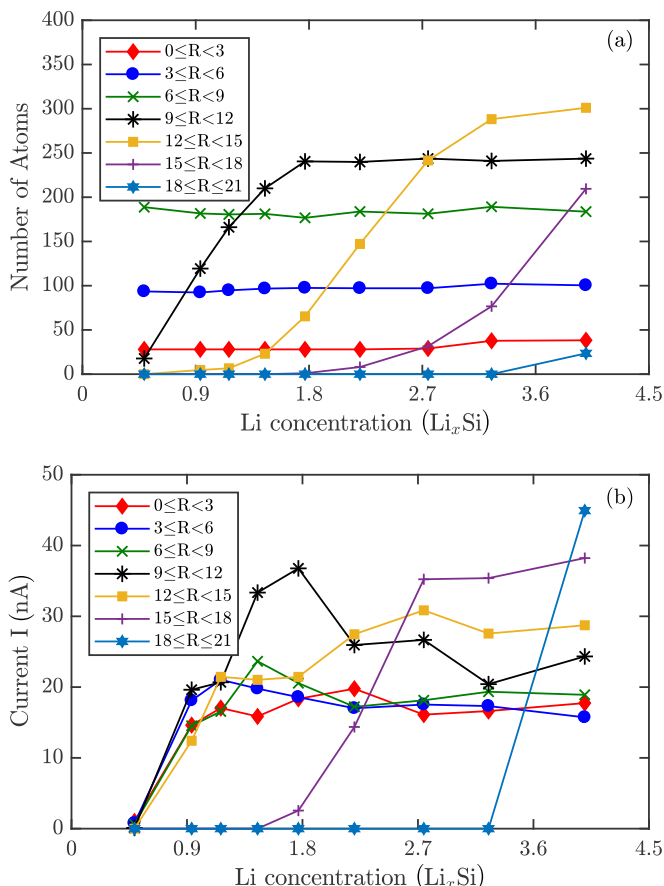
FIG. 12. (a) Total number of atoms (Si and Li) and (b) average electrical current per shell around the center of the Li$_x$Si nanowires with different Li concentrations. The inner and outer radius of the rings are given in the legend (units: Å).

close enough to the conduction band to induce a decent current. At larger concentrations, the metallic character of lithium becomes apparent, leading to a notable current flow around the Fermi energy. When focusing on the inner rings shown in Fig. 12 (0 Å ⩽ R < 3 Å, 3 Å ⩽ R < 6 Å, and 6 Å ⩽ R < 9 Å), it can be seen that both the number of atoms as well as the current magnitude remain approximately stable, with little dependence on the Li concentration. Considering the total number of atoms, this is not surprising at small x, as Li is only distributed at the surface of the NWs. However, at higher concentrations, Li also enters the core of the NW, but the total number of atoms does not vary. Si atoms drift outwards to make space for the incoming Li. As a consequence, the current in these rings is not significantly modified. The lithium ions have a more important impact on the rings situated close to the surface. At first, the number of atoms in the surface ring (9 Å ⩽ R < 12 Å) rapidly increases, as does the electrical current. When the maximum number of atoms that can be accommodated in this ring is reached, the current exhibits a peak, before decreasing. At this point the next outermost ring (12 Å ⩽ R < 15 Å) takes over, giving rise to an additional current channel. This behavior repeats itself for the next lithiation rings (15 Å ⩽ R < 18 Å and

18 Å ⩽ R ⩽ 21 Å). The fact that conductive channels first appear at the surface might limit the electrical performance of Si NW-based anodes as such paths are more sensitive to interface roughness [46]. This effect is out of the scope of this paper as it would require the construction of several samples per Li concentration and longer structures. The opening of electrically conductive channels during the lithiation process follows a steplike behavior, as the penetration of Li ions, but the direction of propagation is different: The Li front moves toward the center of the NW shell after shell, while the current channels appear at the surface of the lithiated NW, one after the other.

IV. CONCLUSION

In this paper, we have investigated the structural as well as the electronic properties of Si NW for different lithium concentrations with the help of density-functional theory calculations and quantum transport simulations. The Si NWs have been lithiated until reaching a concentration of Li$_{4.4}$Si. Relevant properties have been determined at each step during this process.

Introducing Li atoms into crystalline Si systems occurs step-by-step, each Si hexagonal shell being successively lithiated. A clear lithiation front is observed, as in experiments. The inserted Li particles donate on average $0.8e$ of their charge to the surrounding Si atoms, thus weakening the Si-Si bonds till the Li front can penetrate further into the highly crystalline NW core. At the end of the lithiation process, the volume of the NW has quadrupled and the Si network has become fully amorphous. During delithiation, the Li ions remain homogeneously distributed at all concentration levels, eliminating the steplike behavior found in the first lithiation cycle. Even after fully delithiating the Si network, Li ions stay inside the structure (0.13 per Si atom), which leads to a volume increase of 13%, as compared to the original crystalline structure and a capacity loss.

Experiments showed that the introduction of an SiO$_2$ shell [47,48] could be beneficial and reduce the observed volume expansion. Further calculations could shed light on this behavior and be used to minimize the volume expansion of the NW.

From subsequent quantum transport simulations, it can be concluded that the introduction of lithium atoms into the silicon core modifies the current flow distribution. Whereas electrons mainly flow through the center of the wire in a pure crystalline Si NW, the major contributions shift toward the surface upon lithiation. The impact of this current redistribution should be investigated in larger NW structures, where interface roughness and other relevant scattering mechanisms, e.g., electron-phonon, are considered.

[1] P. Poizot, S. Laruelle, S. Grugeon, L. Dupont, and J. Tarascon, Nature **407**, 496 (2000).

[2] M. Armand and J.-M. Tarascon, Nature **451**, 652 (2008).

[3] J.-M. Tarascon and M. Armand, *Materials For Sustainable Energy: A Collection of Peer-Reviewed Research and Review Articles from Nature Publishing Group* (World Scientific, Singapore, 2011), pp. 171–179.

[4] N. Nitta, F. Wu, J. T. Lee, and G. Yushin, Mater. Today **18**, 252 (2015).

[5] Y. Xie, M. Naguib, V. N. Mochalin, M. W. Barsoum, Y. Gogotsi, X. Yu, K.-W. Nam, X.-Q. Yang, A. I. Kolesnikov, and P. R. Kent, J. Am. Chem. Soc. **136**, 6385 (2014).

[6] H. Wu and Y. Cui, Nano Today **7**, 414 (2012).

[7] B. Dunn, H. Kamath, and J.-M. Tarascon, Science **334**, 928 (2011).

[8] L.-F. Cui, Y. Yang, C.-M. Hsu, and Y. Cui, Nano Lett. **9**, 3370 (2009).

[9] S. W. Lee, M. T. McDowell, J. W. Choi, and Y. Cui, Nano Lett. **11**, 3034 (2011).

[10] C.-M. Park, J.-H. Kim, H. Kim, and H.-J. Sohn, Chem. Soc. Rev. **39**, 3115 (2010).

[11] C. K. Chan, H. Peng, G. Liu, K. McIlwrath, X. F. Zhang, R. A. Huggins, and Y. Cui, *Materials for Sustainable Energy: A Collection of Peer-Reviewed Research and Review Articles from Nature Publishing Group* (World Scientific, Singapore, 2011), pp. 187–191.

[12] L.-F. Cui, R. Ruffo, C. K. Chan, H. Peng, and Y. Cui, Nano Lett. **9**, 491 (2008).

[13] J. Rohrer, A. Moradabadi, K. Albe, and P. Kaghazchi, J. Power Sources **293**, 221 (2015).

[14] H. Yang, S. Huang, X. Huang, F. Fan, W. Liang, X. H. Liu, L.-Q. Chen, J. Y. Huang, J. Li, T. Zhu *et al.*, Nano Lett. **12**, 1953 (2012).

[15] X. H. Liu, H. Zheng, L. Zhong, S. Huang, K. Karki, L. Q. Zhang, Y. Liu, A. Kushima, W. T. Liang, J. W. Wang *et al.*, Nano Lett. **11**, 3312 (2011).

[16] M. K. Chan, C. Wolverton, and J. P. Greeley, J. Am. Chem. Soc. **134**, 14362 (2012).

[17] A. Jain, Y. Shin, and K. A. Persson, Nat. Rev. Mater. **1**, 15004 (2016).

[18] A. F. Kohan, G. Ceder, D. Morgan, and C. G. Van de Walle, Phys. Rev. B **61**, 15019 (2000).

[19] C. Ma, X. Shao, and D. Cao, J. Mater. Chem. **22**, 8911 (2012).

[20] K. Zhao, W. L. Wang, J. Gregoire, M. Pharr, Z. Suo, J. J. Vlassak, and E. Kaxiras, Nano Lett. **11**, 2962 (2011).

[21] G. Ceder, Y.-M. Chiang, D. Sadoway, M. Aydinol, Y.-I. Jang, and B. Huang, Nature **392**, 694 (1998).

[22] G. Kresse and J. Furthmüller, Phys. Rev. B **54**, 11169 (1996).

[23] G. Kresse and J. Furthmüller, Comput. Mater. Sci. **6**, 15 (1996).

[24] A. A. Mostofi, J. R. Yates, Y.-S. Lee, I. Souza, D. Vanderbilt, and N. Marzari, Comput. Phys. Commun. **178**, 685 (2008).

[25] Quantum ATK 2017.1, https://www.synopsys.com/silicon/quantumatk.html.

[26] P. E. Blöchl, Phys. Rev. B **50**, 17953 (1994).

[27] W. H. Press, S. A. Teukolsky, W. T. Vetterling, and B. P. Flannery, *Numerical Recipes, 3rd ed.: The Art of Scientific Computing* (Cambridge University Press, Cambridge, 2007).

[28] A. Stukowski, Modell. Simul. Mater. Sci. Eng. **18**, 015012 (2009).

[29] A. Pedersen, P. A. Khomyakov, and M. Luisier, Phys. Rev. Appl. **4**, 034005 (2015).

[30] T. Bunjaku and M. Luisier, Phys. Rev. Mater. **3**, 034001 (2019).

[31] M. S. Islam and C. A. Fisher, Chem. Soc. Rev. **43**, 185 (2014).

[32] R. Teki, M. K. Datta, R. Krishnan, T. C. Parker, T.-M. Lu, P. N. Kumta, and N. Koratkar, Small **5**, 2236 (2009).

[33] C. K. Chan, H. Peng, G. Liu, K. McIlwrath, X. F. Zhang, R. A. Huggins, and Y. Cui, Nat. Nanotech. **3**, 31 (2008).

[34] G. Henkelman, B. P. Uberuaga, and H. Jónsson, J. Chem. Phys. **113**, 9901 (2000).

[35] S. Smidstrup, A. Pedersen, K. Stokbro, and H. Jónsson, J. Chem. Phys. **140**, 214106 (2014).

[36] W. Tang, E. Sanville, and G. Henkelman, J. Phys.: Condens. Matter **21**, 084204 (2009).

[37] M. Luisier, A. Schenk, W. Fichtner, and G. Klimeck, Phys. Rev. B **74**, 205323 (2006).

[38] Á. Szabó, Dissipative quantum transport simulations in two-dimensional semiconductor devices from first principles, Ph.D. thesis, ETH Zürich, 2016.

[39] D. Bauer, T. Bunjaku, A. Pedersen, and M. Luisier, J. Appl. Phys. **122**, 055105 (2017).

[40] Y. Kubota, M. C. S. Escaño, H. Nakanishi, and H. Kasai, J. Appl. Phys. **102**, 053704 (2007).

[41] H. Kim, K. E. Kweon, C.-Y. Chou, J. G. Ekerdt, and G. S. Hwang, J. Phys. Chem. C **114**, 17942 (2010).

[42] A. Pedersen, M. Bieri, M. Luisier, and L. Pizzagalli, Phys. Rev. Appl. **7**, 054012 (2017).

[43] A. Marcolongo and N. Marzari, Phys. Rev. Mater. **1**, 025402 (2017).

[44] J. P. Perdew, Int. J. Quant. Chem. **28**, 497 (1985).

[45] M. Nolan, S. O'Callaghan, G. Fagas, J. C. Greer, and T. Frauenheim, Nano Lett. **7**, 34 (2007).

[46] A. Svizhenko, P. W. Leu, and K. Cho, Phys. Rev. B **75**, 125417 (2007).

[47] S. Sim, P. Oh, S. Park, and J. Cho, Adv. Mater. **25**, 4498 (2013).

[48] M. T. McDowell, S. W. Lee, I. Ryu, H. Wu, W. D. Nix, J. W. Choi, and Y. Cui, Nano Lett. **11**, 4018 (2011).